# High-throughput Prediction of Thermodynamic Stabilities of Dopant-defect Clusters at Misfit Dislocations in Perovskite Oxide Heterostructures

Chloe Marzano and Pratik P. Dholabhai*

*School of Physics and Astronomy*
*Rochester Institute of Technology*
*Rochester, NY 14623*

* Email: pratik.dholabhai@rit.edu

## Abstract

Complex oxide heterostructures and thin-films have emerged as promising candidates for diverse applications, wherein interfaces formed by joining two different oxides play a central role in novel properties that are not present in the individual components. Lattice mismatch between the two oxides lead to the formation of misfit dislocations, which often influence vital material properties. In oxides, doping is used as a strategy to improve properties, wherein inclusion of aliovalent dopants lead to formation of oxygen vacancy defects. At low temperatures, these dopants and defects often form stable clusters. In semi-coherent perovskite oxide heterostructures, the stability of such clusters at misfit dislocations while not well understood, is anticipated to impact interface-governed properties. Herein, we report atomistic simulations elucidating the influence of misfit dislocations on the stability of dopant-defect clusters in $SrTiO_3$/$BaZrO_3$ heterostructures. SrO–BaO, SrO–$ZrO_2$, BaO–$TiO_2$, and $ZrO_2$–$TiO_2$ interfaces having dissimilar misfit dislocation structures were considered. High-throughput computing was implemented to predict the thermodynamic stabilities of 275,610 dopant-defect clusters in the vicinity of misfit dislocations. Misfit dislocation structure of the given interface and corresponding atomic layer chemistry play a fundamental role in influencing the thermodynamic stability of geometrically diverse clusters. A stark difference in cluster stability is observed at misfit dislocations lines and intersections as compared to the coherent terraces. These results offer an atomic scale perspective of the complex interplay between dopants, point defects, and extended defects, which is necessary to comprehend the functionalities of perovskite oxide heterostructures.

## 1. Introduction

Complex oxide heterostructures, a class of materials fabricated by marrying two dissimilar oxides, offers opportunities to develop next-generation devices with desired functionalities. As compared to their parent oxides, oxide heterostructures exhibit emerging properties that can be attributed to the newly formed heterointerface,[1] which offers diverse modes to introduce non-homogeneity in the heterostructure. Complex oxide thin films and heterostructures have found applications in a wide range of technologies that include solid oxide fuel cells (SOFCs),[2,3] radiation tolerant nuclear materials,[4,5] information storage,[6,7] batteries,[8] and catalysts.[9] Since nanostructured devices have a high interface-to-volume ratio, in the majority of these applications, heterointerfaces play a vital role in dictating novel behavior.

Depending on the lattice mismatch between the two crystalline oxides, their heterostructures have varying degree of strain at the heterointerface, which often alters their atomic and electronic structure as well as their overall stability.[10] In semi-coherent oxide heterostructures, depicted in **Figure 1**, misfit dislocations originate at the heterointerface to mitigate the misfit strain between the two mismatched oxides. Since misfit dislocations are responsible for controlling key material properties,[3,11,12,13] studies investigating their role in semi-coherent oxide heterostructures has received increasing focus. Experimental studies focused on elucidating the atomic scale structure of misfit dislocations are limited because studying and characterizing the role of individual column of atoms at the heterointerface is challenging. Nonetheless, owing to their fundamental role in dictating material properties, recent computational and experimental studies have focused on thorough investigation of the structure-property relationships at misfit dislocations in oxides.

Perovskite oxides have wide-ranging applications and are some of the most extensively studied materials. Recently, heterostructures based on perovskite oxides have gained popularity due to their versatility in various technologies.[14] Similar to semiconductor technologies, doping is characteristically used to tune ionic, electronic, and optical properties of emerging perovskite oxides.[15,16] Depending on the desired application, doping can enhance magnetic,[17] ionic,[18] electronic,[19] optical, and catalytic[20] properties of perovskite oxides. The added impurities are likely to segregate at surfaces as well as homophase and heterophase boundaries, an outcome that predominantly depends on size mismatch and charge interactions,[21] formation of space-charge layers at interfaces,[22] and on growth conditions and post-deposition annealing procedures.[23]

However, there are cases where segregation at these boundaries might not be energetically and thermodynamically favorable. As a result, dopants would be excluded from the interface region in such cases. Since these segregated additives could lead to deleterious effects on the material stability and performance, numerous studies have focused on understanding the segregation behavior of dopants and associated defects in complex oxides.

**Figure 1.** *Atomic visualization of misfit dislocations in mismatched perovskite oxides. Misfit dislocations emerge at the interface to mitigate the strain due to different lattice constants of the film and the substrate.*

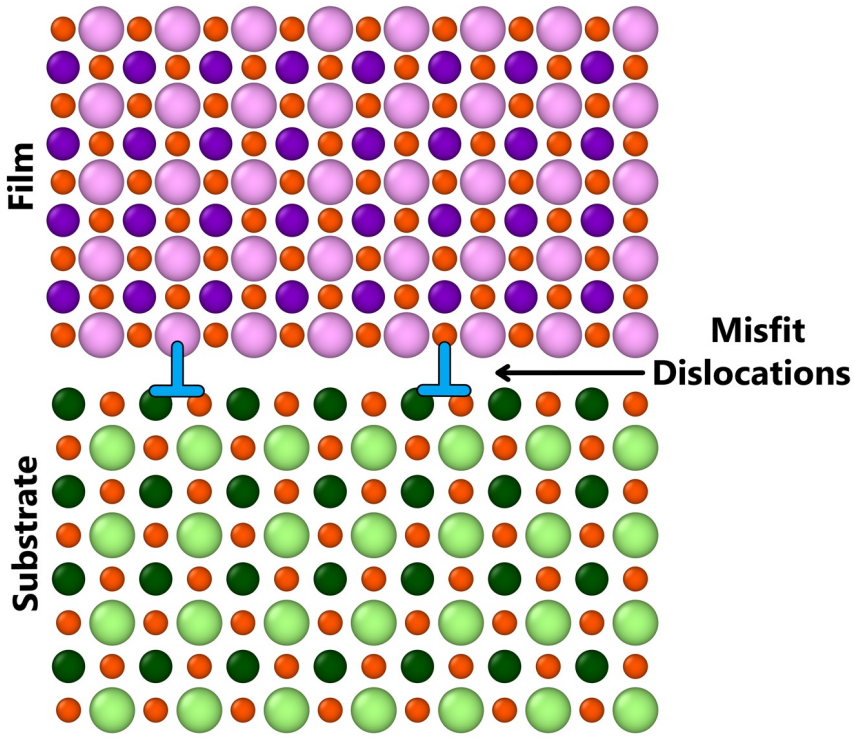


$SrTiO_3$ (STO)[24] and $BaZrO_3$ (BZO) are perovskite oxides often doped to tune their functionality for wide-ranging applications. In a typical $ABO_3$ perovskite oxide lattice, due to the flexibility in composition, dopants can replace either *A*-site, *B*-site, or *O*-site ions. Since the current work is primarily focused on fundamental aspects of ionic transport in STO/BZO heterostructures, we will restrict our discussion to acceptor doping (*p*-type).[25] A wide variety of aliovalent dopants can be added to improve the properties of perovskites. In acceptor doping of perovskites, the *B*-site cations, either $Ti^{4+}$ in STO or $Zr^{4+}$ in BZO, could be replaced with trivalent dopants. Acceptor doping has been extensively studied in STO[26] and BZO[27], as they have a net effective charge that

affects the electroneutrality condition, and thereby the defect equilibria leading to formation of oxygen vacancies. For instance, acceptor trivalent dopants Gd,[28] Er,[28] La,[28] Al,[29] Cr,[29] Mn,[28,30,31] Pr,[32] Y,[28,33] Fe,[34,35,36] and Sm[28,37] at *B*-site in STO have been investigated for ionic conductivity applications since the charge compensating mechanism is the formation of oxygen vacancies. However, dopants such as Cr, Pr, Mn, and Fe also exhibit mixed valence, which could lead to emergence of novel properties in addition to ionic conductivity applications.[38] In addition, *A*-site doping has also been studied for other applications but will not be considered in this work. In perovskite oxides, defects could typically introduce ligand holes, which could further lead to altered magnetic properties. For instance, such behavior has been reported in STO.[39,40,41] However, we strictly focus on studying the role of defects (oxygen vacancies) that are formed to maintain the defect equilibria after trivalent dopant incorporation. Since the current work is focused on the stability of clusters for understanding interface governed ionic transport, emphasis on oxygen vacancies and dopants is rational since vacancy diffusion mechanism is the primary mechanism for ionic conductivity in oxide electrolytes.[2,3] Similar to STO, a wide variety of trivalent dopants such as Al,[42] La,[42] Lu,[42] Sc,[27,42,43] Y,[27,42,43] In,[27,42,43] Pr,[43] Nd,[42,43] Sm,[42,43] Eu,[43] Gd,[27,42,43] Tb,[43] Dy,[43] Ho,[43] Er,[43] Tm,[43] and Yb[43] have been studied on the *B*-site (acceptor doping) in BZO.

Because acceptor doping has been extensively used to improve the properties of STO and BZO, it is imperative to understand the basic role of trivalent dopants in these materials. More importantly, substitution of trivalent dopants on the *B*-site lead to formation of oxygen vacancies, and subsequent formation of dopant-defect clusters, which is not well understood.[28] It is important to note that the aforementioned studies on trivalent dopants in STO and BZO are mostly performed for a single material, either STO or BZO. Besides, most studies do not offer fundamental details of the mutual existence of dopants and defects. To the best of our knowledge, there are no studies in the literature that investigate the role of dopants and defects at heterointerfaces in STO/BZO heterostructures, let alone at misfit dislocations. Since STO[44] and BZO[27] have several technologically applications, oxide heterostructures synthesized using either of them as one of the parent systems has garnered recent interest. For instance, STO-based heterostructures have applications in high temperature superconductors and ferroelectrics,[44] enhanced ionic transport for SOFC electrolytes,[3,45,46,47] solid-state electric-double-layer transistor,[48] model systems to study radiation damage evolution and fast ion conduction.[49,50,51,52]

Since segregation is a thermodynamically driven process, to design next-generation oxide heterostructures, basic knowledge of dopants and how the atomic structure of the heterointerface influences the segregation of added impurities and associated defects will be crucial. Moreover, at semi-coherent oxide heterointerfaces, the behavior of dopants and defects in the vicinity of misfit dislocations is not well understood. One of the main reasons for the lack of understanding is due to the challenges in experimentally visualizing individual dopant atoms and characterizing oxygen vacancies and resolving the structure and chemistry of misfit dislocations. The problem is further compounded as even from a theoretical perspective, simulations that involve density functional theory (DFT) are limited to coherent interfaces to keep the supercell size tractable.[53] As a result, DFT calculations are not optimal to study misfit dislocation structure of semi-coherent heterointerfaces, which necessitate very large supercells. In this regard, atomistic simulations based on empirical interatomic potentials are instrumental in offering atomic scale details of dopants and defects at misfit dislocations in semi-coherent oxide heterostructures.[28,53]

In cases where either STO or BZO is used to fabricate oxide heterostructures, comprehending the role of dopants and defects in influencing the nanomaterial properties would be beneficial. To achieve this goal in the present study, we utilized atomistic simulations in conjunction with high-throughput computing to investigate the thermodynamic stabilities of thousands of dopant-defect clusters in the model system of STO/BZO heterostructure,[54] with emphasis on misfit dislocations and interface region. We studied geometrically diverse clusters at SrO–BaO, SrO–$ZrO_2$, BaO–$TiO_2$, and $ZrO_2$–$TiO_2$ interfaces having dissimilar misfit dislocation structures.[54] The main goal of this work is to offer atomic scale insights pertaining to the thermodynamic preference of dopants-defect clusters and shed light on their behavior near differing misfit dislocation structures in STO/BZO heterostructures.

## 2. Methodology

Atomistic simulations with 3D periodic boundary conditions (PBC) were conducted within the framework of Large-scale Atomic/Molecular Massively Parallel Simulator (LAMMPS).[55] The simulations are based on energy minimization using a classical Born-like description of an ionic solid. Parameterized Buckingham[56] pair potentials are utilized to describe the two-body short-range interactions, whereas interactions due to the long-range Coulombic (electrostatic) forces were calculated by means of Ewald's method.[57] Since the Coulomb potential has an effectively

infinite range, Particle-Particle Particle-Mesh (PPPM) Ewald summation,[58] which is one of the methods in LAMMPS, was utilized to compute the total potential energy. This method effectively switches the summation from direct space into reciprocal (or Fourier) space and incorporates Fast Fourier Transforms (FFT) to compute the total Coulombic potential energy for an effectively infinite crystal when the simulation enforces periodic boundary conditions.[58] Parameters for the Buckingham pair potential as derived by Busker *et al*.[59] and Zacate *et al.*[60] were used for $Sr^{2+}$, $Ti^{4+}$, $Ba^{2+}$, $Zr^{4+}$, $O^{2-}$, and $Gd^{3+}$. These interatomic potential parameters were chosen as all the divalent, trivalent, and tetravalent cation interactions were fitted against the same $O^{2-} – O^{2-}$ potential.

We constructed the atomic models of STO/BZO heterostructure for the experimentally observed cube-on-cube orientation relationship, wherein $(001)_{STO}||(001)_{BZO}||$interface and $[010]_{STO}||[010]_{BZO}$.[61] Since the experimental lattice parameters are $a_{STO} = 3.905$ Å and $a_{BZO} = 4.197$ Å, and the lattice parameters computed in this work are within 0.3% of the experimental values, the lattice mismatch (~7.0%, computed with respect to a BZO substrate) resulting from this orientation relationship is accommodated via the formation of misfit dislocations at the heterointerface. In these atomic models, 14 unit cells of STO were matched with 13 unit cells of BZO to ensure a heterostructure with negligible amount of extrinsic strain. Via cleaving STO at either the neutral SrO or $TiO_2$ layer and BZO at either the neutral BaO or $ZrO_2$ layer, there are four combinations of heterointerfaces possible, namely SrO–BaO, SrO–$ZrO_2$, BaO–$TiO_2$, and $ZrO_2$–$TiO_2$. Due to PBC, whenever one heterointerface is constructed for simulation, another is formed at the top and bottom of the corresponding supercell. This, coupled with stoichiometric preservation, means that in our simulations interfaces always come as inseparable pairs, as seen in **Figure 2**. For these fully stoichiometric heterostructures, constant temperature and pressure (NPT) simulations were performed using the conjugate gradient method for internal coordinate and stress minimization using the Nosé-Hoover thermostat at 0 K and zero pressure to obtain a relaxed structure free from internal stresses. The 0 K relaxed structures were further annealed at 800 K.

The methodology used in this work has been successfully used to study structure-property relationships at misfit dislocations,[28,49,50,51,54,62] surfaces,[63] and grain boundaries[64] in complex oxides, wherein the relative trends obtained from atomistic simulations are in good qualitative agreement with those obtained from density functional theory (DFT) calculations. Importantly, this approach has offered reasonable comparison with experiments and assisted in further interpreting experimental results.[52] Consequently, the current methodology should have adequate

physical fidelity to offer physically meaningful trends that are in qualitative agreement with DFT calculations. In addition, we recently computed the electronic and atomic structure of misfit dislocations at $CeO_2$/MgO heterostructures using DFT[10] and offered comparison with the atomic structure obtained using atomistic simulations.[62] We uncovered that the atomic structure and qualitative trends for dopant-defect cluster stability predicted using DFT and atomistic simulations agree very well. This agreement not only validates the current approach, but also reveals that the underlying assumptions of the method remain truthful.

The defect reaction governing the addition of trivalent dopants to $TiO_2$ (STO) or $ZrO_2$ layer (BZO) can be expressed in Kröger–Vink notation as:

$$\boldsymbol{M_2O_3 \xrightarrow{BO_2} 2M'_B + V_O^{\cdot\cdot} + 3O_O^{\times}} \qquad \boldsymbol{(1)}$$

where $\boldsymbol{V_O^{\cdot\cdot}}$, $\boldsymbol{B}$, and $\boldsymbol{M}$ correspond to the oxygen vacancy, *B*-site cations (either $Ti^{4+}$ or $Zr^{4+}$) in perovskites, and trivalent dopants ($Gd^{3+}$), respectively. Owing to ionic compensation, this reaction indicates that the substitution of two *B*-site cations with trivalent dopants will result in the formation of one oxygen vacancy. Using the final annealed heterostructures, two locations for the host cations (either $Ti^{4+}$ or $Zr^{4+}$) were systematically replaced with $Gd^{3+}$ dopants and an oxygen vacancy was created, forming what we will refer to as dopant-defect clusters, as shown in **Figure 3**. The entire system was then minimized at constant volume. That is, after swapping with gadolinium dopants and oxygen vacancy incorporation, energy minimization of the entire system was performed wherein the ionic positions were allowed to fully relax before computing relative energies. In this approach, the relative cluster energy is computed as the change in total energy of the system due to the addition of dopants and resulting oxygen vacancy formation at different locations. That is, for every doped heterostructure, the cluster stability (segregation energy) is computed as the difference in energy between the cluster at the most favorable location and the respective site. A simplified equation for computing the cluster stability is given by

$$\boldsymbol{E_{cluster}(x) = E_{total}(x) - E_{total}^{min}} \qquad (2)$$

where $\boldsymbol{E_{cluster}(x)}$ is the relative thermodynamic stability of the cluster at location $\boldsymbol{x}$, $\boldsymbol{E_{total}(x)}$ is the total energy of the respective heterostructure with a cluster placed at location $\boldsymbol{x}$, and $\boldsymbol{E_{total}^{min}}$ is

the total energy for the heterostructure for the cluster at the most favorable location, that is, the lowest total energy across all clusters. Thus, it is the relative driving force for the cluster to reside at a given site compared to the most favorable site (which, for a given case, is taken as the zero of energy).

**Figure 2.** *(a) The SrO–BaO and $TiO_2$–$ZrO_2$ interfaces are always paired (b) The SrO–$ZrO_2$ and $TiO_2$–BaO interfaces are always paired. When PBC are introduced and the crystal structure is repeated above and below itself, it creates an additional interface, which is always paired with the interface at the center, regardless of how many layers of either oxide is added.*

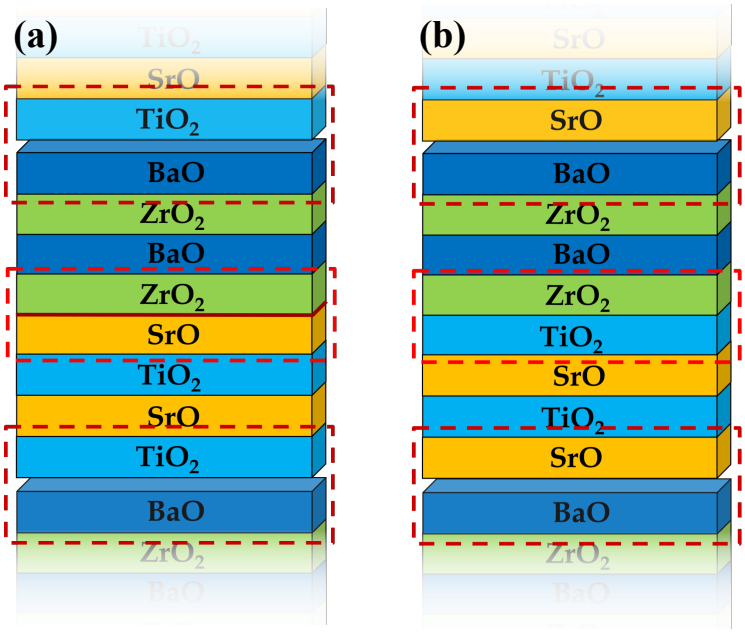


Dopant-defect clusters shown in **Figure 3** can form anywhere within the bulk of either material or anywhere in the vicinity of the interface. As such, the number of permutations for all possible clusters that could form within the entire heterostructure is astronomically large, leading to roughly 4.2 million clusters. We imposed additional constraints when generating the clusters to reduce these permutations down to more realistic numbers while still maintaining a large enough span for data collection. Firstly, only one side of each heterointerface was doped at a time, either the STO size or the BZO side, and clusters were strictly not allowed to cross the interface plane. In addition, clusters were generated within 3 unit cells (6 layers) above the interface; we are only focusing on clusters' interactions with each respective heterointerface, and anything beyond

roughly 6 layers is essentially within the bulk of the material. Dopant atoms were replaced no more than 1 unit cell apart from each other, such that the maximum distance between them is $\sqrt{3}a$. Once the dopants were placed, the oxygen vacancies were generated at either first or second nearest neighbors to either of the dopants. Additionally, clusters were only generated at every other unit cell location when iterating laterally through the planes parallel to the interface, which further reduced our total permutations by about 75%. In total, for each side of the given interface, we generated approximately 34,000 clusters, resulting in a net total of 275,610 dopant-defect cluster permutations. To ensure that the entire space of allowable structures was spanned, every single vacancy location and possible cluster geometries associated with this vacancy and two dopants were created and tested. Further details about cluster visualization and data interpretation are given in the next section. The ultimate goal of the work is to gain insights into the distribution of where these clusters tend to form with respect to each interface and corresponding misfit dislocations. Finding the relative distributions of stable clusters will further offer insights into the location preference of oxygen vacancies to form at the interface, which will further inform researchers focused on studying the role of oxygen vacancies in ionic transport near the interface regions.

**Figure 3.** *Three among several possible dopant-defect cluster configurations are illustrated. The gadolinium dopants (light green) replaced the titanium atoms (light blue) on the STO lattice. Missing oxygen ions (oxygen vacancies) from where it would normally be in an ideal crystalline lattice are shown by dashed circles.*

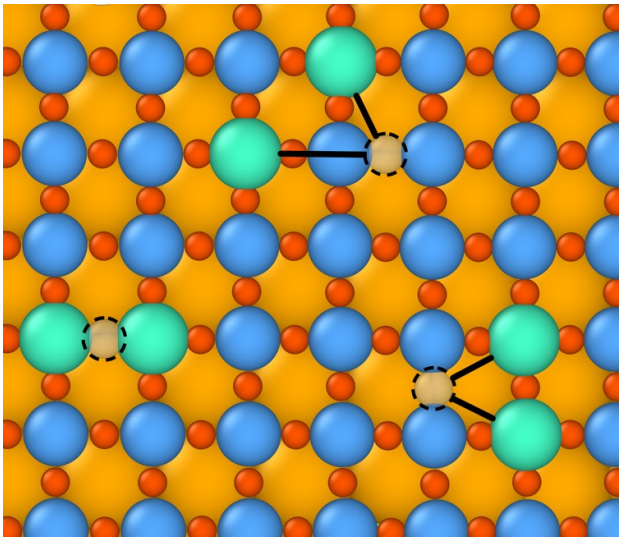

## 3. Results & Discussion

**Figure 4.** *Side view of misfit dislocations for (a) SrO–$ZrO_2$ (b) $TiO_2$–BaO (c) SrO–BaO and (d) $TiO_2$–$ZrO_2$ interfaces. Misfit dislocations in (a) SrO–$ZrO_2$ and (b) $TiO_2$–BaO interfaces can clearly be seen in the center, where the atoms do not form a perfect lattice. Misfit dislocations in (c) SrO–BaO interface are toward the edge, where cation–cation and anion–anion nearest neighbors across the interface repel each other. Misfit dislocations in (d) $TiO_2$–$ZrO_2$ interface are not clearly distinguishable in this view. Gold, blue, dark blue, green, and red spheres correspond to Sr, Ti, Ba, Zr, and O atoms, respectively. Oxygen ions deeper within the lattice do not line up with those near the front; oxygen ions are laterally shifted from one another as they go deeper into the structure. As explained later in the main text, this is due to the* ⟨110⟩ *dislocation patterns at this interface.*

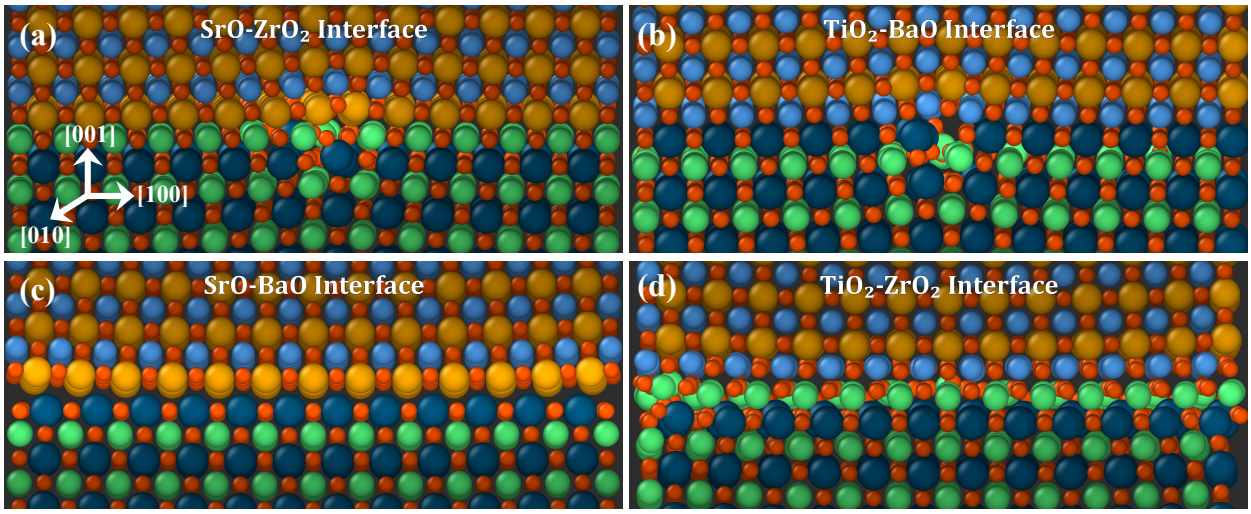


For the experimentally observed cube-on-cube orientation relationship in STO/BZO heterostructures, four different types of interfaces could form depending on the interface layer chemistries involved in the formation of the interface. **Figure 4** created using OVITO (Open Visualization Tool)[65] depicts the side views of minimized and subsequently annealed structures of SrO–$ZrO_2$, $TiO_2$–BaO, SrO–BaO, and $ZrO_2$–$TiO_2$ interfaces. In the interface pairing of SrO–$ZrO_2$ (**Figure 4a**) and $TiO_2$–BaO (**Figure 4b**), the dislocations are evident in the center of the heterostructure. On the contrary, at the SrO–BaO (**Figure 4c**) and $TiO_2$–$ZrO_2$ (**Figure 4d**), the dislocations are less obvious. This is due to the varying densities of anions and cations on each of the neutral layers being joined at the heterointerface and direction of the Burgers vector as

explained later. In both SrO–$ZrO_2$ and $TiO_2$–BaO interfaces, there is a 2:3 ratio between cations and anions, which closely mimics the ratios seen in a typical perovskite oxide lattice. However, in SrO–BaO and $TiO_2$–$ZrO_2$ interfaces, there is a 2:2 and 2:4 ratio of cations to anions, respectively. In the latter cases, there is an increased chance that the two cations or two anions sit directly atop one another, leading to chemical frustration at the interface. In the former cases, the $ZrO_2$ layer mimics the $TiO_2$ layer that is normally joined with the SrO layer, and likewise the $TiO_2$ layer mimics the $ZrO_2$ layer that is normally joined with the BaO layer. However, unequal number of columns on the two sides of the heterointerface imply that for all the four interfaces, neighborhoods with favorable (cations–anions) and unfavorable (anions–anions or cations–cations) interactions will exist that influence the misfit dislocation structure.

The annealed heterostructures can be further analyzed to discern the misfit dislocation structures that are formed the four interfaces. A top-down view of the misfit dislocation patterns across the four interface planes are offered in **Figure 5**, wherein only one layer from either side of the heterointerface is shown. To distinguish misfit dislocation lines and intersections from coherent regions, atoms are color-coded based on their centrosymmetry parameter, which is a unitless parameter characterizing the degree of deviation of a given atom from a perfect crystal lattice. In SrO–$ZrO_2$ (**Figure 5a**) and $TiO_2$–BaO (**Figure 5b**) interfaces, the centrosymmetry parameter is large along the [100] and [010] directions (square patterns), which correspond to the misfit dislocations. This is in contrast with the patterns observed in SrO–BaO (**Figure 5c**) and $TiO_2$–$ZrO_2$ (**Figure 5d**) interfaces, wherein the centrosymmetry parameter is fairly large in most regions. However, the dislocation patterns can be discerned, with the SrO–BaO interface having the largest centrosymmetry parameter along the [100] and [010] directions (square patterns), and the $TiO_2$–$ZrO_2$ interface exhibit that effect in the [110] and [110] directions (diamond pattern). A closer inspection of the interface atomic arrangement reveals that the coherent terraces in all the four interfaces exhibit favorable electrostatic interactions, wherein cations from one side of the heterointerace are favorably bonded with anions from the other side and vice versa. At misfit dislocation lines and intersections, regions with chemical frustration are observed in all the cases. Such atomic scale details are vital, since chemically frustrated regions are often conducive to defect formation.

**Figure 5.** *A top-down view of the dislocation patterns throughout the (a) SrO–$ZrO_2$ (b) $TiO_2$–BaO (c) SrO–BaO and (d) $TiO_2$–$ZrO_2$ interface planes. Atoms are color-coded based on their centrosymmetry parameter to distinguish dislocation and coherent terraces. The first set of interfaces in (a) and (b) form highly localized dislocation patterns owing to the dislocation network in the* ⟨100⟩ *direction. In the second set of interfaces in (c) and (d), the former shows a similar dislocation pattern in* ⟨100⟩ *direction, whereas the latter exhibits a dislocation network in* ⟨110⟩ *direction.*

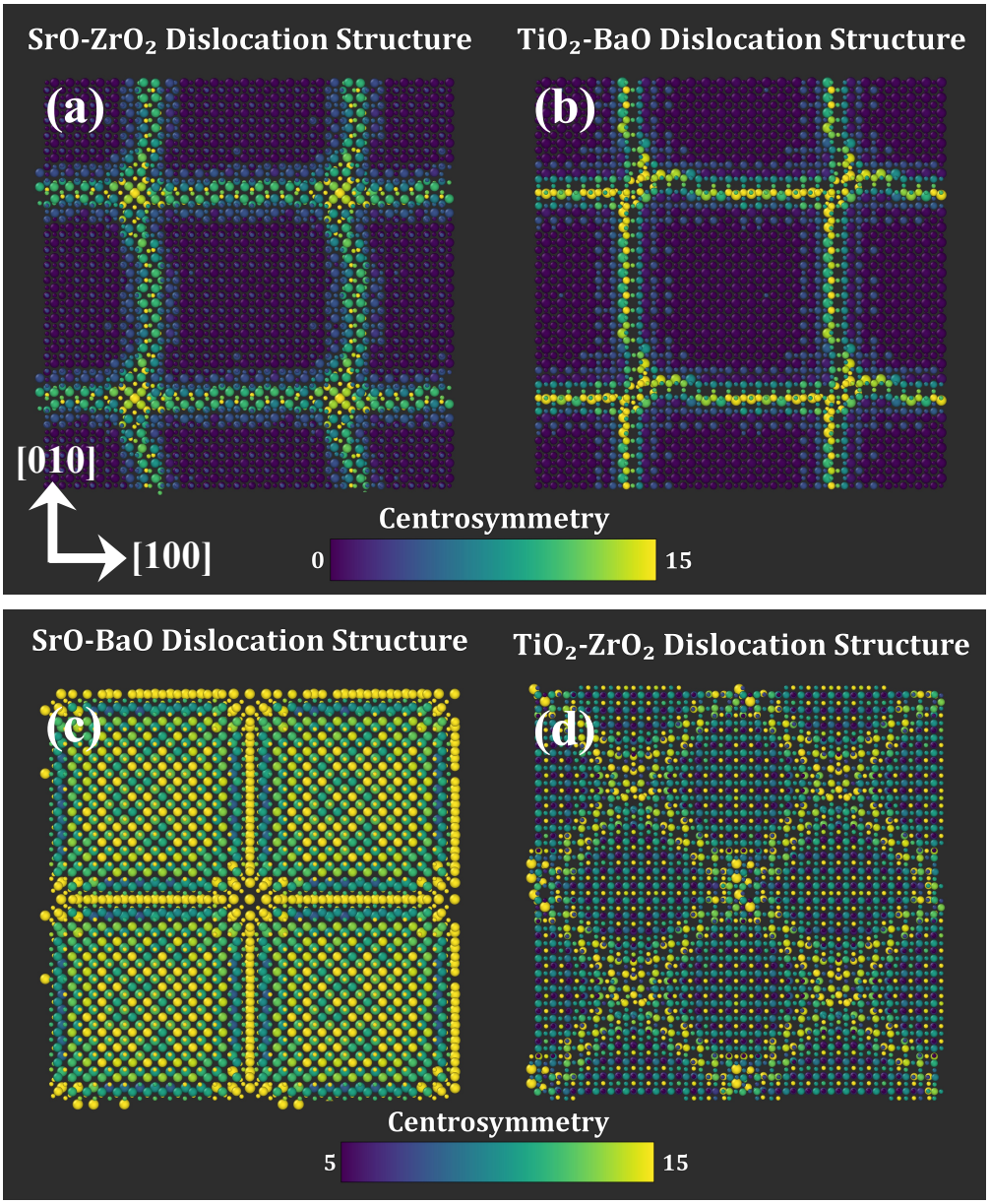

Based on the dislocation patterns visible in **Figure 5**, the direction of the Burgers vector for each of the dislocations can be deduced. A Burgers vector of $\vec{b} = \langle 100 \rangle$ is predicted for SrO–$ZrO_2$, $TiO_2$–BaO, and SrO–BaO interfaces, whereas for the $TiO_2$–$ZrO_2$ interface, a misfit dislocation structure with Burgers vector of $\vec{b} = \langle 110 \rangle$ is predicted. This prediction is in agreement with the qualitative prediction reported using a heuristic approach.[54] While experiments have reported perovskite-perovskite heterostructures with cube-on-cube epitaxy,[66] dependence of the misfit dislocation structure on interface layer chemistry is not well understood.[53] Since these differing misfit dislocation structures as a function of interface chemistry are expected to influence interface-governed properties,[3,10,13,28,49] these results reveal the importance of understanding such fundamental aspects of interface formation.

**Figure 6.** *Relative energy distributions for each interface configuration. Each curve represents the relative population of clusters at given energy. Color scheme in the violin plots is representative of the respective material. Curves on the bottom half of each violin plot are only meant to indicate distributions for the lower half of the interface; they are not negative values.*

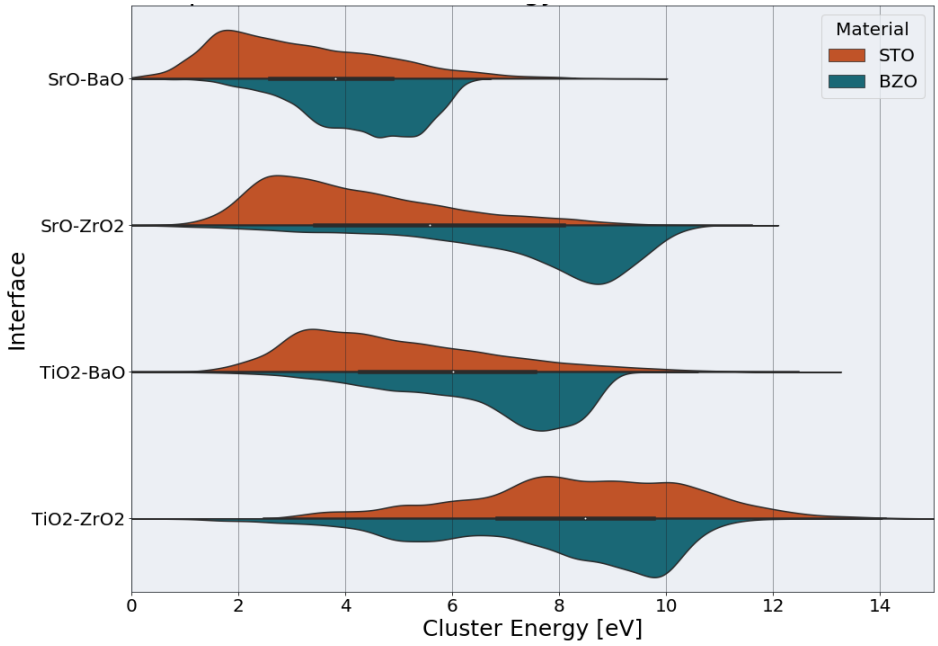


After each dopant-defect cluster configuration was minimized and its thermodynamic stability was calculated, the main goal as well as challenge was to interpret the data to uncover the

fundamental trends governing the interaction of dopant-defect clusters with misfit dislocations at each heterointerface. As a first method of analysis, we grouped the cluster energies for each side of each interface into a histogram, which was then smoothed out using a kernel density estimate curve, to see the relative populations of cluster stabilities given in **Figure 6**. Generally, clusters on the STO side of each interface had lower groupings of energies than those on the BZO side. One caveat is that these cluster energies should not be directly compared between different interfaces, since these are only relative distributions scaled by the lowest energy cluster of each group, so information about their absolute formation energies is unknown.

Visualizing and interpreting the vast amount of data generated via high-throughput computing was challenging since there are a few degrees of freedom for every cluster. That is, two dopant atoms and one oxygen vacancy, all positioned along three axes near each interface plane. Finding how the energies are distributed spatially is therefore nontrivial, since there is no obvious way to assign a single atomic position to each cluster. The first method we used for assigning position to a cluster was to simply use the position of oxygen vacancy defect in that cluster, since these sites are what allow ions to conduct through the lattice and arguably have a higher importance. However, this meant that not only were there around 30 to 40 clusters stacked directly on top of one another, since many different clusters can all share the same vacancy location, but also the distribution of energies for a single vacancy location was quite widespread. This indicated that the location of dopants was important as well. In order to assign a weight to the dopant positions, we used a linear interpolation between the vacancy site and the average position of both dopant atoms, specifically using an interpolation parameter of $t = \frac{1}{3}$ in the equation shown below,

$$\boldsymbol{r(t) = (1 - t) \cdot r_{vacancy} + t \cdot \frac{1}{2}\left(r_{dopant1} + r_{dopant2}\right)} \qquad \textbf{(3)}$$

where $\boldsymbol{r(t)}$, $\boldsymbol{r_{vacancy}}$, and $\boldsymbol{r_{dopant}}$ are the locations of the cluster, oxygen vacancy, and dopants, respectively. This strategy had the effect of spreading apart the clusters that were located directly on top of one another while also allowing the assigned position of each cluster to be influenced by the oxygen vacancy and two dopant atoms. Though this is not the only method of visualization, we chose this approach since it produced consistent results.

**Figure 7.** *Relative dopant-defect cluster energies throughout the SrO–$ZrO_2$ heterointerface (a) STO side is doped and (b) BZO side is doped. Relative dopant-defect cluster energies throughout the $TiO_2$–BaO heterointerface (c) STO side is doped and (d) BZO side is doped. Energy scale is given below the panel. Interface orientation is same for all materials as given in (a).*

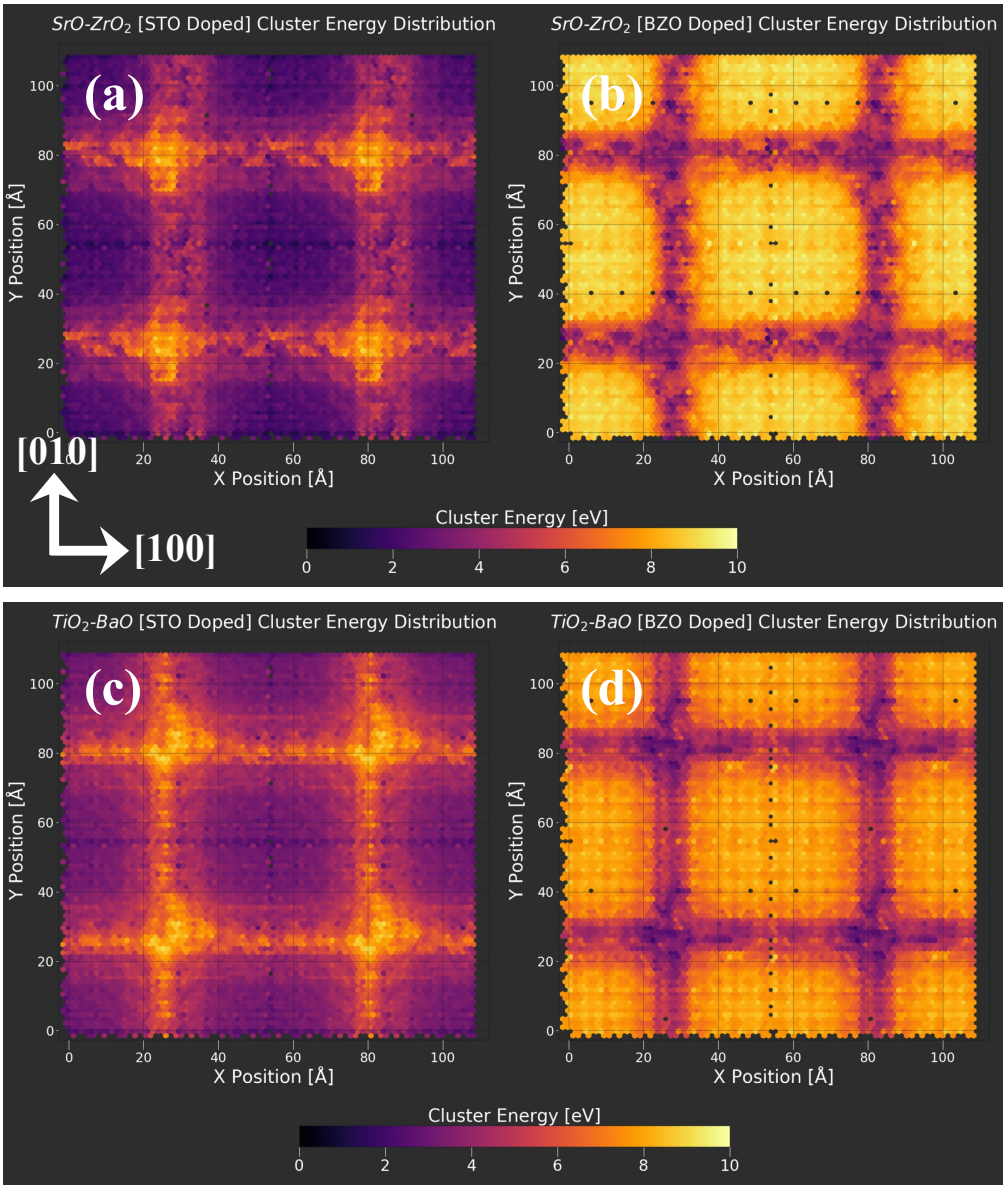


Relative dopant-defect cluster energy stabilities computed using **Equation 2** are given for SrO–$ZrO_2$ interface with STO side and BZO side doped in **Figure 7a** and **7b**, respectively. Energy stabilities for $TiO_2$–BaO interface with STO side and BZO side doped are shown in **Figure 7c** and **7d**, respectively. Analogously, **Figure 8** offers the cluster energy stabilities for SrO–BaO interface

when STO side (**Figure 8a**) and BZO side (**Figure 8b**) is doped as well as $TiO_2$–$ZrO_2$ interface when STO side (**Figure 8c**) and BZO side (**Figure 8d**) is doped. In **Figure 7** and **8**, the interface normal direction is portrayed so as to draw a clear comparison with **Figure 5**, and more importantly, focus on the behavior of clusters at the interface layers. Since acceptor doping is performed only in $TiO_2$ and $ZrO_2$ layers, in interface configurations wherein SrO or BaO layers are at the interface, doping and inclusion of oxygen vacancies is carried out starting from the second layer at the interface. This is a reasonable approach because it has been shown that two to three layers adjacent to the interface are critical in influencing interface-governed properties. [3,12,13,28] Evidently, the misfit dislocation patterns in **Figure 5** have a strong influence on the cluster stabilities depicted in **Figure 7** and **8**. A common trend uncovered at these interfaces is that the dopant-defect clusters on the STO side of each interface exhibit greater stabilities in the coherent terraces, which reveal their location preference for formation in STO. Conversely, clusters on the BZO side of each interface demonstrate greater stabilities along the dislocation lines and intersections revealing their tendencies to form in this region.

The contrasting patterns observed in **Figure 7** and **8** for cluster stabilities on the STO side as compared to those on the BZO side of the interface results in a sort of mirror image effect. At the atomic scale, this effect can be explained in terms of relative size mismatch between dopant atoms and host atoms, as well as lattice mismatch and nearest neighbor atomic arrangement at the interface. For six coordination, the ionic radiuses of $Sr^{2+}$, $Ti^{4+}$, $Ba^{2+}$, $Zr^{4+}$, and $Gd^{3+}$ are 1.18 Å, 0.61 Å, 1.35 Å, 0.72 Å, and 0.94 Å, respectively.[67] The ionic radius of $Sr^{2+}$and $Ti^{4+}$ is smaller than that of $Ba^{2+}$ and $Zr^{4+}$, respectively. Importantly, the ionic radius of $Gd^{3+}$ is larger than either of the host cation $Ti^{4+}$ and $Zr^{4+}$. As mentioned earlier, the coherent terrace of all interfaces comprises of favorable electrostatic interactions, wherein the atoms across the interface are nicely packed and mostly similar in numbers. This stacking is displayed in **Supporting Information Figure S1** and **S2**, which clearly depicts a single atomic layer on each side of the minimized interface for BZO and STO, respectively. Replacement of larger $Gd^{3+}$ dopants in place of $Ti^{4+}$ (STO side is doped) would result in tensile relaxation in the interface STO layer, leading to a decrease in strain at the heterointerface, as lattice constant of STO (3.905 Å) is smaller than that of BZO (4.197 Å). Decrease in overall strain at the heterointerface due to tensile relaxation will be energetically favorable. Replacing $Zr^{4+}$ (BZO side is doped) with larger $Gd^{3+}$ dopants will also result in tensile relaxation of the interface BZO layer, however, in this case it will increase the strain at the

heterointerface, which will be energetically costly (unfavorable). As a result, dopant-defect clusters exhibit greater stabilities at coherent terraces on the STO (**Figure S2**) side of the interface. This effect is reversed at misfit dislocation lines and intersections, wherein the free space is quite large in the BZO side of the interface as compared to the STO side since there are fewer atoms in BZO (**Figure S1**). Owing to this available free space, tensile relaxation after addition of larger $Gd^{3+}$ dopants is energetically favorable for the BZO side. As a result, dopant-defect clusters demonstrate greater stabilities along the dislocation lines and intersections at BZO side of each interface. At the atomic scale, fundamental structural and interface effects observed herein are expected to influence key interface-governed properties.[7,11,19,21,28,61,66]

The spatial distributions for cluster energies shown in **Figures 7** and **8** are a conglomeration of dopant-defect clusters of all possible configurations given our parameters for generation; there is no consideration for clusters in different orientations or where the oxygen vacancy site lies with respect to the dopant locations. To account for this, we compared the energy distributions for various classifications of cluster types. The way we classified cluster configurations was by considering the nearest neighbor distance from the oxygen vacancy site to each of the two dopant atoms. For example, if the first dopant atom was a second nearest neighbor and the second dopant was a third nearest neighbor to the oxygen vacancy site, then the cluster would be classified as a Type **2–3**. We focused our analysis on Types **1–1**, **1–2**, and **2–2** clusters, since clusters with at least a third nearest neighbor had significantly shifted energy distributions, indicating lower favorability, which has also been reported for other oxide interfaces.[10,28,63]

Relative thermodynamic stabilities for clusters of various types in each of the four heterointerfaces are depicted in **Figure 9**. Evidently, when the dopant-defect cluster energy distributions are plotted for **1–1**, **1–2**, and **2–2** clusters, a general trend is uncovered wherein the distributions shift rightward for higher order nearest neighbor clusters. This effect is somewhat subtle, but when comparing the mean and median of each distribution, both increase monotonically with nearest neighbor order. This indicates that clusters of the Type **1–1** are the most favorable to form. However, it is worth noting that while the energy distributions indicate higher favorability in a one-to-one comparison, clusters of Type **1–1** have the lowest multiplicity due to combinatorics. For instance, for a given vacancy site in the $TiO_2$ or $ZrO_2$ layer, due to perovskite symmetry, there is only, at most, one distinct **1–1** cluster that can be formed. In general, as the

classification ranges from **1–1** to **1–2** and to **2–2**, distributions tend to shift towards higher formation energies, indicating that vacancies prefer to form not very far from the dopant atoms.

**Figure 8.** *Relative dopant-defect cluster energies throughout the SrO–BaO heterointerface (a) STO side is doped and (b) BZO side is doped. Relative dopant-defect cluster energies throughout the $TiO_2$–$ZrO_2$ heterointerface (c) STO side is doped and (d) BZO side is doped. Energy scale is given below the panel. Interface orientation is same for all materials as given in (a).*

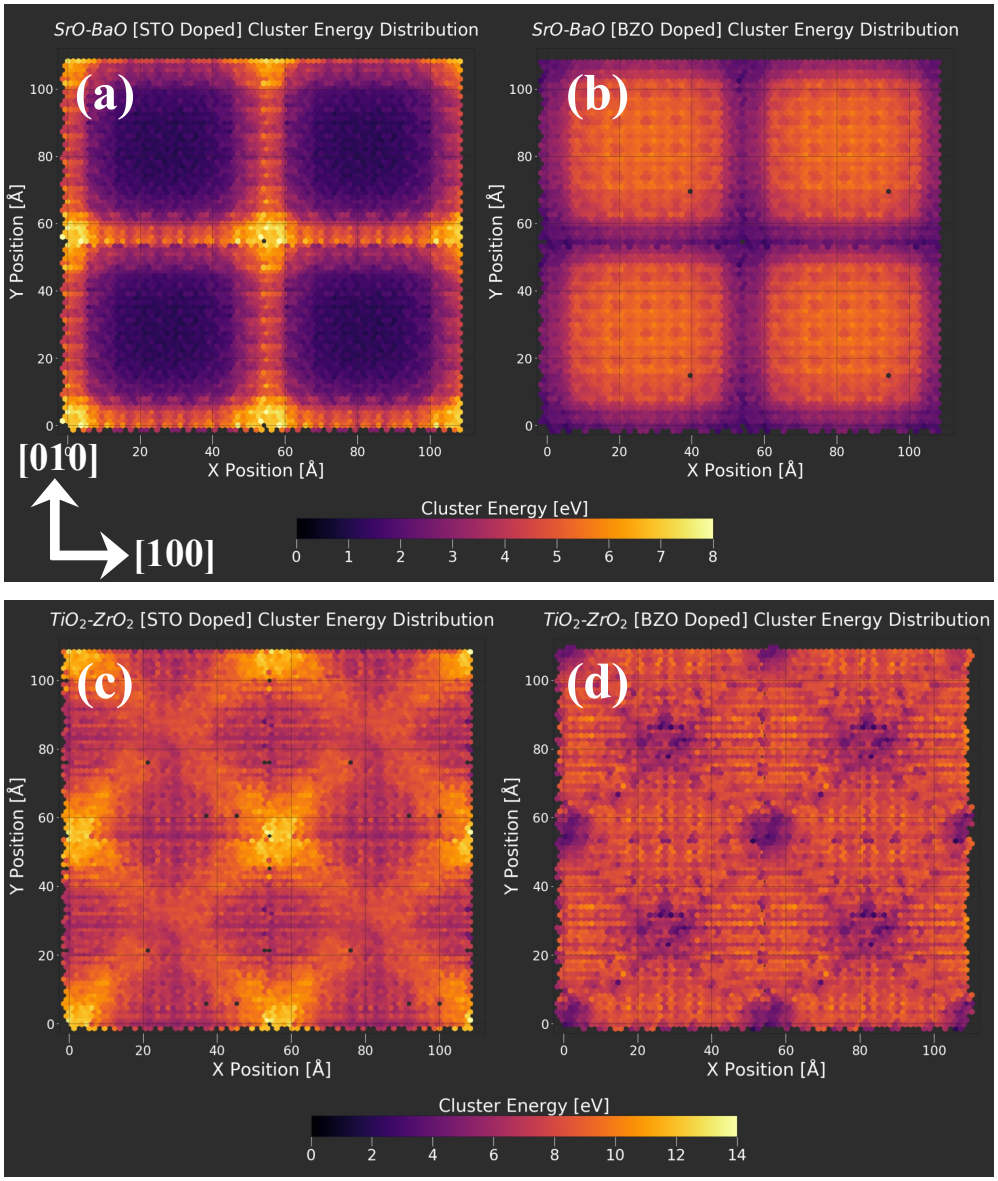

**Figure 9.** *Relative energy distributions for different types of clusters in (a) SrO–$ZrO_2$ (b) $TiO_2$–BaO (c) SrO–BaO and (d) $TiO_2$–$ZrO_2$ interface. Plot details are same as in* ***Figure 6****.*

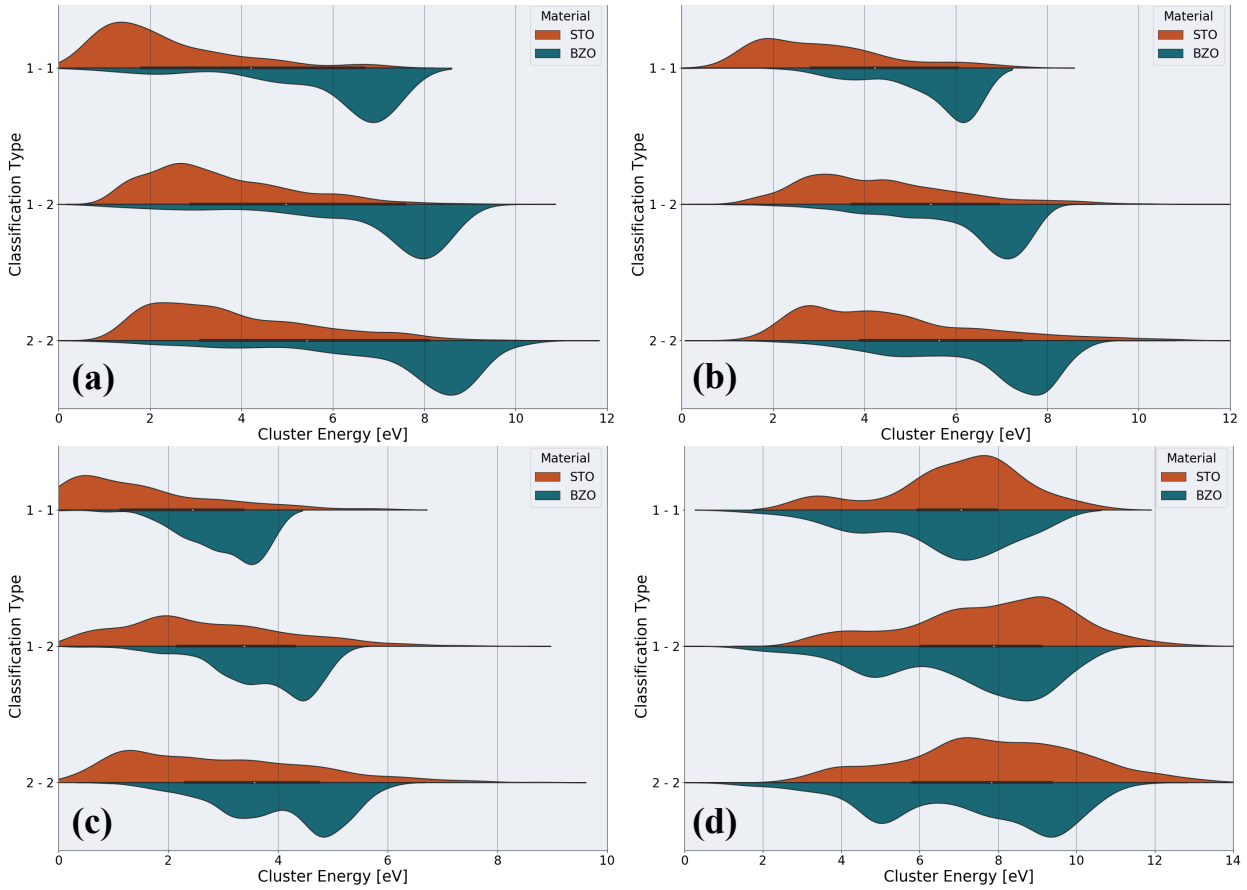


Throughout this study, only one dopant-defect cluster has been considered at any given time, not accounting for the influence of other clusters. That is, a rather dilute limit of dopant fraction is utilized. At higher dopant fractions, it is possible that numerous disparate clusters agglomerate at the interface. It is probable that more intricate atomic landscape is present at the interface. For instance, for a given **1–1** arrangement, the two dopants therein could have additional oxygen vacancies at nearby locations, or the oxygen vacancy in this **1–1** cluster arrangement could have additional dopants at second or third nearest neighbors. Furthermore, to identify a particular cluster, we have strictly located oxygen vacancies and dopants on the same side of the interface. In reality, it is quite possible that oxygen vacancies present on the STO side of the interface could be nearest neighbors to dopants on the BZO side and vice versa. Such scenarios would further

influence the cluster stabilities. In general, cluster-cluster interaction would influence the stabilities of coexisting clusters. Nonetheless, by conducting a thorough investigation of isolated dopant-defect clusters, we have predicted the thermodynamics of cluster formation, which could be further utilized to understand their behavior at higher dopant concentrations.

Though the interface has more free space than the grain interior to accommodate larger dopants and minimize the elastic energy, a remarkable result uncovered in this work is that not all sites at the interface between two mismatched oxides are conducive for segregation of dopants and defects. This is in stark contrast with dopant segregation tendencies reported at perovskite surfaces,[68,69,70] and oxide surfaces in general,[71] where dopant size and charge mismatch lead to surface segregation owing to elastic and electrostatic interactions. At perovskite surfaces, only few distinctly probable sites are available to dopants, most of which are favorable for segregation, [68,69,70,72] which is not the case for heterointerfaces of perovskite heterostructures reported herein. Cationic sites for dopant segregation inside and outside the dislocation cores in perovskite $BaSnO_3$ have also been reported, indicating that dislocations are generally conducive for dopant segregation.[73] The key difference in perovskites heterostructures studied here are the presence of misfit dislocations, wherein several dissimilar sites are available for segregation,[28] some of which are not conducive for segregation due to interface layer chemistry and mismatch strain as well as atomic scale structure of the misfit dislocations. In general, since perovskite oxide heterostructures have gained popularity for novel materials and devices, current results reveal that fundamental understanding of dopants and defects segregation in the vicinity of misfit dislocations would be beneficial. More importantly, since interface-governed properties of perovskite oxides are strongly influenced by dopants and defects at the interface, high-throughput framework reported in this work offers a novel approach to comprehend their thermodynamics at the atomic scale.

## 4. Conclusions

Since oxide heterostructures exhibit a wide array of functionalities that originate at the heterointerface, their rational design at the atomic scale and nanoscale requires *a priori* knowledge of interface stability and the fundamental role of dopants and defects at interfaces. In this work, atomistic simulations were used to investigate the atomic scale structure of misfit dislocations in STO/BZO heterostructures for varying termination chemistries and study the interplay between extended defects, dopants, and vacancy defects. A high-throughput framework was developed to

screen the thermodynamic stability of thousands of dopant-defect clusters at the interface, which was found to fundamentally depend on the atomic scale structure of misfit dislocations and interface layer chemistry of the given heterostructure. Contrasting patterns for cluster stabilities are observed, wherein clusters exhibit greater stabilities in coherent terraces on STO side of the interface, whereas they prefer misfit dislocation lines and intersections on the BZO side. These contrasting patterns results in a mirror image effect, which is understood in terms of size mismatch between host and dopant, lattice mismatch, and nearest neighbor atomic stacking at the interface. Dopant-defect clusters having oxygen vacancy at first nearest neighbor to the two dopants are uncovered to be most favorable, with the distributions shifting toward higher formation energies at larger nearest neighbor distances, revealing a strong binding between the dopants and defects. Atomic scale details offered herein for cluster stabilities in the vicinity of misfit dislocations are essential to comprehend the functionalities of mismatched perovskite oxide heterostructures.

**Conflicts of interest**

There are no conflicts to declare.

**Supporting Information:** Interface layer atomic arrangements for STO and BZO.

**Acknowledgements**

This work is supported by the National Science Foundation (NSF) CAREER Award grant number DMR-2042311 in the Division of Materials Research. The authors gratefully acknowledge computing resources from Research Computing at Rochester Institute of Technology. This work used Extreme Science and Engineering Discovery Environment (XSEDE), which is supported by NSF grant number ACI-1548562.

**References**


[1] Christensen, D. V.; Chen, Y.; Esposito, V.; Pryds, N. The role of oxide interfaces in highly confined electronic and ionic conductors. *APL Mater*. **2019**, 7, 013101.

[2] Kilner J. A.; Burriel, M. Materials for Intermediate-Temperature Solid-Oxide Fuel Cells. *Annu. Rev. Mater. Res*., **2014**, 44, 365–393.

[3] Fabbri, E.; Pergolesi, D.; Traversa, E. Ionic Conductivity in Oxide Heterostructures: The Role of Interfaces. *Sci. Technol. Adv. Mater*., **2010**, 11, 054503.

[4] Uberuaga, B. P.; Martinez, E.; Bi, Z.; Zhuo, M.; Jia, Q.; Nastasi, M.; Misra, A.; Caro, A. Defect Distributions and Transport in Nanocomposites: A Theoretical Perspective. *Mater. Res. Lett*., **2013**, 1, 193–199.

[5] Sickafus, K. E.; Grimes, R. W.; Valdez, J. A.; Cleave, A.; Tang, M.; Ishimaru, M.; Corish, S. M.; Stanek, C. R.; Uberuaga, B. P. Radiation-induced Amorphization Resistance and Radiation Tolerance in Structurally Related Oxides. *Nat. Mater*., **2007**, 6, 217–223.

[6] Hwang, H. Y.; Iwasa, Y.; Kawasaki, M.; Keimer, B.; Nagaosa, N.; Tokura, Y. Emergent Phenomena at Oxide Interfaces. *Nat. Mater.,* **2012**, 11, 103–113.

[7] Salluzzo, M.; Gariglio, S.; Stornaiuolo, D.; Sessi, V.; Rusponi, S.; Piamonteze, C.; De Luca, G. M.; Minola, M.; Marré, D.; Gadaleta, A. *et al*. Origin of Interface Magnetism in $BiMnO_3/SrTiO_3$ and $LaAlO_3/SrTiO_3$ Heterostructures. *Phys. Rev. Lett*., **2013**, 111, 087204.

[8] Zhu, B.; Fan, L.; Lund, P. Breakthrough Fuel Cell Technology Using Ceria-based Multi-functional Nanocomposites. *Appl. Energy*, **2013**, 106, 163–175.

[9] Wang, J.; Ji, G.; Liu, Y.; Gondal, M. A.; Chang, X. $Cu_2O/TiO_2$ Heterostructure Nanotube Arrays Prepared by an Electrodeposition Method Exhibiting Enhanced Photocatalytic Activity for $CO_2$ Reduction to Methanol. *Catal. Comm*., 2014, 46, 17–21.

[10] Dholabhai, P. P. Oxygen Vacancy Formation and Interface Charge Transfer at Misfit Dislocations in Gd-Doped CeO2/MgO Heterostructures. *J. Phys. Chem. C* **2022**, 126, 11735−11750

[11] Santiso, J.; Roqueta, J.; Bagueś, N.; Frontera, C; Konstantinovic, Z.; Lu, Q.; Yildiz, B.; Martínez, B.; Pomar, A.; Balcells, L. *et al.* Self-Arranged Misfit Dislocation Network Formation upon Strain Release in $La_{0.7}Sr_{0.3}MnO_3/LaAlO_3(100)$ Epitaxial Films under Compressive Strain. *ACS Appl. Mater. Interfaces* **2016**, 8, 16823−16832.

[12] Korte, C.; Peters, A.; Janek, J.; Hesse, D.; Zakharov, N. Ionic conductivity and activation energy for oxygen ion transport in superlattices—the semicoherent multilayer system YSZ($ZrO_2$ + 9.5 mol% $Y_2O_3$)/$Y_2O_3$. *Phys. Chem. Chem. Phys*., **2008**, 10, 4623–4635.

[13] Harrington, G. F.; Cavallaro, A.; McComb, D. W.; Skinner S. J.; Kilner, J. A. The Effects of Lattice Strain, Dislocations, and Microstructure on the Transport Properties of YSZ Films. *Phys. Chem. Chem. Phys*., **2017**, 19, 14319–14336.

[14] Orvis, T.; Cao, T.; Surendran, M.; Kumarasubramanian, H.; Singh Thind, A.; Cunniff, A.; Mishra, R.; Ravichandran, J. Direct Observation and Control of Surface Termination in Perovskite Oxide Heterostructures. *Nano Lett*. **2021**, 21, 4160.

[15] Haque, M. A.; Villalva, D. R.; Hernandez, L. H.; Tounesi, R.; Jang, S.; Baran, D. Role of Dopants in Organic and Halide Perovskite Energy Conversion Devices. *Chem. Mater*. **2021**, 33, 8147.

[16] Liu,Y.; Huang, H.; Xue, L.; Sun, J.; Wang, X.; Xiong, P.; Zhu, J. Recent advances in the heteroatom doping of perovskite oxides for efficient electrocatalytic reactions. *Nanoscale*, **2021**, 13, 19840.

[17] Choudhury, D.; Pal, B.; Sharma, A.; Bhat, S. V.; Sarma, D. D. Magnetization in Electron- and Mn-doped $SrTiO_3$. *Sci. Rep.,* **2013**, 3, 1433.

[18] Maier, R. A.; Randall, C. A. Low-Temperature Ionic Conductivity of an Acceptor-Doped Perovskite: I. Impedance of Single-Crystal $SrTiO_3$. *J. Am. Ceram. Soc*., **2016**, 99 [10] 3350–3359.

[19] Cheng, J.; Wang, Y.; Luo, J.; Yang, K. δ-Doping Effects on Electronic and Energetic Properties of $LaAlO_3/SrTiO_3$ Heterostructure: First-Principles Analysis of 23 Transition-Metal Dopants. *Adv. Mater. Inter.,* **2017**, 4, 1700579.

[20] McFarland, E. W.; Metiu, H. Catalysis by Doped Oxides. *Chem. Rev*., **2013**, 113, 4391–4427.

[21] Lee, W.; Han, J. W.; Chen, Y.; Cai, Z.; Yildiz, B. Cation Size Mismatch and Charge Interactions Drive Dopant Segregation at the Surfaces of Manganite Perovskites. *J. Am. Chem. Soc*., **2013**, 135 [21] 7909–7925.

[22] Shirpour, M.; Rahmati, B.; Sigle, W.; van Aken, P. A.; Merkle, R.; Maier, J. Dopant Segregation and Space Charge Effects in Proton-Conducting $BaZrO_3$ Perovskites. *J. Phys. Chem. C*, **2012**, 116, 2453–2461.

[23] Chung, S.; Kang, S. L.; Dravid, V. P. Effect of Sintering Atmosphere on Grain Boundary Segregation and Grain Growth in Niobium-Doped $SrTiO_3$. *J. Am. Ceram. Soc*., **2002**, 85 [11] 2805–2810.

[24] Pai, Y.; Tylan-Tyler, A.; Irvin, P.; Levy, J. Physics of $SrTiO_3$-based Heterostructures and Nanostructures: A Review. *Rep. Prog. Phys.*, 2018, **81**, 036503.

[25] Luo, W.; Duan, W.; Louie, S. G.; Cohen, M. L. Structural and Electronic Properties of *n*-doped and *p*-doped $SrTiO_3$. *Phys. Rev. B*, **2004**, 70, 214109.

[26] Bowes, P. C.; Baker, J. N.; Irving, D. L. Survey of acceptor dopants in $SrTiO_3$: Factors limiting room temperature hole concentration. *J. American Ceram. Soc.*, **2020**, 103, 1156–11733.

[27] Vera, C. Y. R.; Ding, H.; Peterson, D.; Gibbons, W. T.; Zhou, M.; Ding, D. A mini-review on proton conduction of $BaZrO_3$-based perovskite electrolytes. *J. Phys. Energy*, **2021**, 3, 032019.
[28] Dholabhai, P. P.; Martinez, E.; Uberuaga, B. P. Influence of Chemistry and Misfit Dislocation Structure on Dopant Segregation at Complex Oxide Heterointerfaces. *Adv. Theory Simul*. **2019**, 2, 1800095.
[29] Hui, S.; Petric, A. Electrical Properties of Yttrium-Doped Strontium Titanate under Reducing Conditions. *J. Electro. Soc.*, **2002**, 149, J1–J10.
[30] Ohly, C.; Hoffmann-Eifert, S.; Szot, K.; Waser, R. Electrical Conductivity and Segregation Effects of Doped $SrTiO_3$ Thin Films. *J. Eur. Ceram. Soc.*, **2001**, 21, 1673–1676.
[31] Azamat, D.V.; Badalyan, A.G.; Dejneka, A.; Trepakov, V.A.; Jastrabik, L.; Frait, Z. High-frequency Electron Paramagnetic Resonance Investigation of $Mn^{3+}$ Centers in $SrTiO_3$. *J. Phys. Chem. Solids* **2012**, 73, 822–826.
[32] Yang, H.; Lee, H. S.; Kotula, P. G.; Sato, Y.; Ikuhara, Y.; Browning, N. D. Amphoteric Doping of Praseodymium $Pr^{31}$ in $SrTiO_3$ Grain Boundaries. *Appl. Phys. Lett.*, **2015**, 106, 121904.
[33] Dai, L.; Wu, L.; Li, H.; Hu, H.; Zhuang, Y.; Liu, K. Evidence of the Pressure-induced Conductivity Switching of Yttrium-doped $SrTiO_3$. *J. Phys. Cond. Matt.*, **2016**, 28, 475501.
[34] Merkle R.; Maier, J. Defect Association in Acceptor-doped SrTiO3 : Case Study for $Fe_{Ti}V_O$ and $Mn_{Ti}V_O$. *Phys. Chem. Chem. Phys*., **2003**, 5, 2297–2303.
[35] Dunyushkina, L. A.; Mashkina, E.A.; Nechaev, I. Yu.; Babkina, A. A.; Esina, N. O.; Zhuravlev, B. V.; Demin, A. K. Influence of Acceptor Doping on Ionic Conductivity in Alkali Earth Titanate Perovskites. *Ionics*, 2002, **8**, 293–299.
[36] Azamat, D.V.; Badalyan, A.G.; Dejneka, A.; Trepakov, V.A.; Jastrabik, L.; Frait, Z. High-frequency Electron Paramagnetic Resonance Investigation of $Mn^{3+}$ Centers in $SrTiO_3$. *J. Phys. Chem. Solids* **2012**, 73, 822–826.
[37] Longo, M.; Costa, M. G. S.; Simoes, A. Z.; Rosa, I. L. V.; Santos, C. O. P.; Andres, J.; Longo, E.; Varela, J. A. On the Photoluminescence Behavior of Samarium-doped Strontium Titanate Nanostructures Under UV Light. A Structural and Electronic Understanding. *Phys. Chem. Chem. Phys*., **2010**, 12, 7566–7579.
[38] Tkach, A.; Vilarinho, P. M.; Kholkin, A. L.; Reaney, I. M.; Pokorny, J.; Petzelt, J. Mechanisms of the Effect of Dopants and P(O2) on the Improper Ferroelastic Phase-Transition in SrTiO3. *Chem. Mater*., **2007**, 19, 26, 6471–6477.
[39] Potzger, K.; Osten, J.; Levin, A. A.; Shalimov, A.; Talut, G.; Reuther, H.; Arpaci, S.; Bürger, D.; Schmidt, H.; Nestler, T.; Meyer, D. C. Defect-induced ferromagnetism in crystalline SrTiO3. *J. Magn. Magn. Mater*., **2011**, 323, 1551-1562.
[40] Lopez-Bezanilla, A.; Ganesh, P.; Littlewood. P. B. Plentiful magnetic moments in oxygen deficientSrTiO3. *APL Mater.,* **2015**, 3, 100701.

[41] Ishida, Y.; Eguchi, R.; Matsunami, M.; Horiba, K.; Taguchi, M.; Chainani, A.; Senba, Y.; Ohashi, H.; Ohta, H.; Shin, S. Coherent and Incoherent Excitations of Electron-Doped SrTiO3. *Phys. Rev. Lett*., **2008**, 100, 056401.

[42] Gilardi, E.; Fabbri, E.; Bi, L.; Rupp, J. L. M.; Lippert, T.; Pergolesi, D.; Traversa, E. Effect of Dopant−Host Ionic Radii Mismatch on Acceptor-Doped Barium Zirconate Microstructure and Proton Conductivity. *J. Phys. Chem. C* **2017**, 121, 9739−9747.

[43] Han, D.; Shinoda, K.; Sato, S.; Majimad, M.; Tetsuya Uda, T. Correlation between electroconductive and structural properties of proton conductive acceptor-doped barium zirconate. J. *Mater. Chem. A*, **2015**, 3, 1243.

[44] Pai, Y.; Tylan-Tyler, A.; Irvin, P.; Levy, J. Physics of $SrTiO_3$-based Heterostructures and Nanostructures: A Review. *Rep. Prog. Phys.*, 2018, **81**, 036503.

[45] Sillassen, M.; Eklund, P.; Pryds, N.; Johnson, E.; Helmersson, U.; Bøttiger, J. Low-temperature Superionic Conductivity in Strained Yttria-stabilized Zirconia. *Adv. Funct. Mater*., **2010**, 20, 2071–2076.

[46] Garcia-Barriocanal, J.; Rivera-Calzada, A.; Varela, M.; Sefrioui, Z.; Iborra, E.; Leon, C.; Pennycook, S. J.; Santamaria, J. Colossal Ionic Conductivity at Interfaces of Epitaxial $ZrO_2$:$Y_2O_3$/$SrTiO_3$ Heterostructures. *Science*, **2008**, 321, 676–680.

[47] Yang, S. M.; Lee, S.; Jian, J.; Zhang, W.; Lu, P.; Jia, Q.; Wang, H.; Noh, T. W.; Kalinin, S. V.; MacManus-Driscoll, J. L. Strongly Enhanced Oxygen Ion Transport Through Samarium-doped $CeO_2$ Nanopillars in Nanocomposite Films. *Nature Comm*. **2015**, 6, 8588.

[48] Tsuchiya, T.; Terabe, K.; Aono, M. All-solid-state Electric-double-layer Transistor Based on Oxide Ion Migration in Gd-doped $CeO_2$ on $SrTiO_3$ Single Crystal. *Appl. Phys. Lett*., **2013**, 103, 073110.

[49] Dholabhai, P. P.; Pilania, G.; Aguiar, J. A.; Misra, A.; Uberuaga, B. P. Termination Chemistry-driven Dislocation Structure at $SrTiO_3$/MgO Heterointerfaces. *Nature Comm*. **2014**, 5, 5043.

[50] Dholabhai, P. P.; Martinez, E.; Brown, N. T.; Uberuaga, B. P. On the Mobility of Carriers at Semi-coherent Oxide Heterointerfaces. *Phys. Chem. Chem. Phys.*, **2017**, 19, 23122.

[51] Dholabhai, P. P.; Aguiar, J. A.; Misra, A.; Uberuaga, B. P. Defect Interactions with Stepped $CeO_2$/$SrTiO_3$ Interfaces: Implications for Radiation Damage Evolution and Fast Ion Conduction. *J. Chem. Phys.*, **2014**, 140, 194701.

[52] Aguiar, J. A.; Dholabhai, P. P.; Bi, Z.; Jia, Q.; Fu, E.; Wang, Y.; Aoki, T.; Zhu, J.; Misra, A.; Uberuaga, B. P. Linking Interfacial Step Structure and Chemistry with Locally Enhanced Radiation-Induced Amorphization at Oxide Heterointerfaces. *Adv. Mater. Inter*. **2014**, 1, 1300142.

[53] Dholabhai, P. P.; Uberuaga, B. P. Beyond Coherent Oxide Heterostructures: Atomic-scale Structure of Misfit Dislocations. *Adv. Theory Simul.* **2019**, 2, 1900078.

[54] Pilania, G.; Dholabhai, P. P.; Uberuaga, B. P. Role of Symmetry, Geometry, and Termination Chemistry on Misfit Dislocation Patterns at Semicoherent Heterointerfaces. *Matter*, **2020**, 2, 1324–1337.

[55] Plimpton, S. Fast Parallel Algorithms for Short-range Molecular Dynamics. *J. Comput. Phys*., **1995**, 117, 1–19.

[56] Buckingham, R. A. The Classical Equation of State of Gaseous Helium, Neon and Argon. *Proc. R. Soc. London, Ser. A*, **1938**, 168, 264.

[57] Ewald, P. P. Evaluation of Optical and Electrostatic Lattice Potentials. *Ann. Phys*., **1921**, 64, 253–287.

[58] Harvey, M. J.; De Fabritiis, G. An Implementation of the Smooth Particle Mesh Ewald Method on GPU Hardware. *J. Chem. Theory Comp*., **2009**, 5, 2371–2377.

[59] Busker, G.; Chroneos, A.; Grimes, R. W.; Chen, I. Solution Mechanisms for Dopant Oxides in Yttria. *J. Am. Ceram. Soc*., **1999**, 82, 1553–1559.

[60] Zacate, M. O.; Minervini, L.; Bradfield, D. J.; Grimes, R. W.; Sickafus, K. E. Defect Cluster Formation in $M_2O_3$-doped Cubic $ZrO_2$. *Solid State Ionics*, **2000**, 128, 243–254.

[61] Choudhury, P.R.; Krupanidhi, S.B. Dielectric response of BaZrO3/BaTiO3 and SrTiO3/BaZrO3 superlattices. J. Appl. Phys., **2008**, 104, 114105.

[62] Dholabhai, P. P. Atomic-scale Structure of Misfit Dislocations in CeO2/MgO Heterostructure and Thermodynamic Stability of Dopant-defect Complexes at the Heterointerface. *Phys. Chem. Chem. Phys*. **2019**, 21, 20878.

[63] Dholabhai, P. P.; Perriot, R.; Uberuaga, B. P.; Atomic-Scale Structure and Stability of the Low-Index Surfaces of Pyrochlore Oxides. *J. Phys. Chem. C*, **2016**, 120, 10485.

[64] Dholabhai, P. P.; Aguiar, J. A.; Wu, L.; Holesinger, T. G.; Aoki, T.; Castro, R. H. R; Uberuaga, B. P. Structure and Segregation of Dopant−defect Complexes at Grain Boundaries in Nanocrystalline Doped Ceria. *Phys. Chem. Chem. Phys*. **2015**, 17, 15375.

[65] Stukowski, A. Visualization and analysis of atomistic simulation data with OVITO–the Open Visualization Tool. *Modelling Simul. Mater. Sci. Eng*., **2010**, 18, 015012.

[66] Kuwata, N.; Sata, N.; Saito, S.; Tsurui, T.; Yugami, H. Structural and electrical properties of $SrZr_{0.95}Y_{0.05}O_3/SrTiO_3$ superlattices. Solid State Ionics, **2006**, 177, 2347– 2351.

[67] Shannon, R. D. Revised effective ionic radii and systematic studies of interatomic distances in halides and chalcogenides. *Acta Crystallogr., Sect. A: Cryst. Phys., Diffr., Theor. Gen. Crystallogr.* **1976**, *32*, 751.

[68] Lee, W.; Han, J. W.; Chen, Y.; Cai, Z.; Yildiz, B. Cation Size Mismatch and Charge Interactions Drive Dopant Segregation at the Surfaces of Manganite Perovskites. *J. Am. Chem. Soc*. **2013**, 135, 7909.

[69] Chung, S. Y.; Choi, S. Y.; Yoon, H. I.; Kim, H. S.; Bae, H. B. Subsurface Space-Charge Dopant Segregation to Compensate Surface Excess Charge in a Perovskite Oxide. *Angew. Chem. Int. Ed*. **2016**, 55, 9680.

[70] Kim, D.; Hunt, A.; Waluyo, I.; Yildiz, B. Cation deficiency enables reversal of dopant segregation at perovskite oxide surfaces under anodic potential. *J. Mat. Chem. A*, DOI: 10.1039/d2ta09118f

[71] Hasan, Md. M.; Dholabhai, P. P.; Castro, R. H.R.; Uberuaga, B. P. Stabilization of $MgAl_2O_4$ spinel surfaces via doping. *Surf. Sci*. **2016**, 649, 138.

[72] Yoon, H. I.; Lee, D. K.; Bae, H. B.; Jo, G. Y.; Chung, H. S.; Kim, J. G.; Kang, S. L.; Chung, S. Y. Probing dopant segregation in distinct cation sites at perovskite oxide polycrystal interfaces. *Nat. Comm*. **2017**, 8, 1417.

[73] Yun, H.; Prakash, A.; Birol, T.; Jalan, B.; Mkhoyan, K. A. Dopant Segregation Inside and Outside Dislocation Cores in Perovskite $BaSnO_3$ and Reconstruction of the Local Atomic and Electronic Structures. *Nano Lett*. **2021**, 21, 4357.